A LOW DOSE AND IN-VIVO IMAGING SYSTEM BASED ON EQUALLY SLOPED TOMOGRAPHY

Guangzhao Zhou[1, 2]*, *Guohao Du*[2], *Yudan Wang*[2], *Dadong Wang*[1]*, *Tiqiao Xiao*[2]*

[1]Quantitative Imaging, CSIRO Data61, Marsfield, NSW 2122, Australia, [2]Shanghai Institute of Applied Physics, Chinese Academy of Sciences, Shanghai 201800, China.
*Corresponding author: gzzhou@sinap.ac.cn, dadong.wang@csiro.au, tqxiao@sinap.ac.cn

ABSTRACT

High radiation dose impedes the development of in-vivo micro-CT. In this paper, we presents a low dose and fast in-vivo micro computed tomography (micro-CT) system based on equally sloped tomography (EST) technique and the monochromatic synchrotron X-ray source. Comparing with regular CT, the projection number required for our imaging system can be reduced by about 75%. In addition, combining with an X-ray shutter, total exposure time of 4 seconds and about 0.67Gy absorption dose for a set of CT data have been achieved. These results demonstrate that micro-CT with monochromatic synchrotron X-rays has great potential in the investigation into the microstructure evolution inside a small animal for biomedical research.

Index Terms— in-vivo micro-CT, equally sloped tomography, synchrotron radiation, biomedical imaging

1. INTRODUCTION

Synchrotron radiation based micro-CT (SR-MCT) has a long history and extensive applications in many fields ranging from biomedicine to material science [1-5]. Due to the high brightness of the 3rd generation synchrotron radiation, Phase Contrast X-ray Microtomography (PMCT) has the potential for in-vivo three dimensional imaging for the study of the microstructure of soft tissues inside small animals [6]. However, there is a major challenge which reduces the experimental efficiency and prevents PMCT from becoming an in-vivo imaging tool. It is how to reduce or eliminate the radiation damage. According to the previous study, the dose threshold for radiation-induced lung damage is around 10-15 Gy [7]. To achieve high resolution, PMCT requires a large number of projections, which implies high radiation dose and long data acquisition time. This means that it is difficult to observe the microstructure dynamics inside a live animal, and meanwhile control the radiation dose at an acceptable level.

High temporal resolution can be obtained using white synchrotron X-ray beam for *in-vivo* MCT [8]. However, it is difficult to acquire accurate quantitative information such as the density using white beam [4]. Recently, a high resolution 4D in-vivo CT based on monochromatic synchrotron X-ray has been developed [9, 10]. Dubsky used simultaneous algebraic reconstruction technique (SART) for the reconstruction to observe the tissue motion of a mouse lung [9]. However, the projection number was up to 400 and the spatial resolution was 20 μm. Sera observed the dynamic process of the tissue motion using the traditional filter back projection algorithm (FBP) with the exposure time of each projection up to 40 ms [10]. In addition, artifacts were introduced due to the sample movement during exposure. With the FBP, a large number of projections are inevitable, which means high radiation dose could be delivered in the sample.

In this paper, equally sloped tomography (EST) is employed to develop a low dose and fast synchrotron *in-vivo* micro-CT system [11]. The system consists of a millisecond X-ray shutter, a multi-dimensional sample stage and a high resolution X-ray detector. The equally sloped tomography (EST) was developed independently for 3D reconstruction, which can evidently reduce the projection number compared to FBP algorithm without the loss of image quality [12]. With 200 total projections and 20 ms exposure time for each, about 0.67Gy absorption dose has been achieved. The system has been opened to users and some results have been achieved [13]. Experiments show that the *in-vivo* micro-CT has achieved high resolution images with low radiation dose.

2. THE IMAGING SYSTEM

2.1 The experimental set-up

At the X-ray Imaging and Biomedical Application Beamline (BL13W1) of Shanghai Synchrotron Radiation Facility (SSRF) - a state of the art 3rd generation 3.5GeV SR facility, synchrotron X-rays are emitted from a 1.9T 8-period hybrid-type wiggler, with a critical energy of 15.4keV [14]. The X-ray beam size at the sample position (34 m from the source, 20keV) is 48 mm horizontally and 5.3 mm vertically. The main optical component is a fixed-exit double crystal monochromator (DCM) cooled by liquid nitrogen. Two sets of Si(111) (8.0 to 38.0keV) and Si(311) (38.0 to 72keV) orientation crystals can be exchanged on line.

Fig. 1 shows the experimental set-up of the low dose and fast imaging system at the beamline. The hardware at the end station mainly consists of three parts, the millisecond X-ray shutter, the multi-dimensional sample stage and X-ray detectors. The shutter was designed by the staff of BL13W1 which was made of two 15 mm thick tungsten carbide blades. By shifting the blades in and out of the X-ray beam path, the shutter's opening time as short as 10 ± 2ms has

been achieved. The sample stage can rotate freely, whereas only from -45° to 135° was selected for the data acquisition. Four different types of X-ray detectors with effective pixel size from 0.17 μm to 24 μm are available at BL13W1.

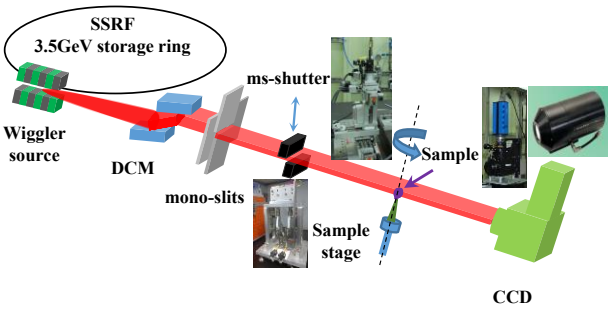

Fig. 1. The schematic layout of the low dose and fast imaging system.

2.2 The EST reconstruction algorithm

The EST reconstruction technique is a Fourier based iterative algorithm which requires that the projections are collected by equally sloped angles, while equally angled projections are employed in the traditional tomographic methods (such as FBP and ART). Combining the pseudo-polar fast Fourier transform (PPFFT) and an iterative algorithm [15], the EST algorithm achieves high quality reconstructions by iterating back and forth between the real and reciprocal spaces.

The 2D PPFFT and its inversion were developed to build an accurate Fourier transform relation between an object in Cartesian grid and its Fourier slices in pseudo-polar grid. As shown in Fig. 2, the object is an N×N pixel array in Cartesian grid. Its PPFFT represents a set of 2N lines and each line has 2N grid points, whereas each line represents a Fourier slice. The 2N lines are divided into a basically horizontal (BH) group and a basically vertical (BV) group. The BH group is defined as $y = sx$, where $|s| \le 1$, and BV group is defined as $x = sy$, where $|s| \le 1$. Instead of the polar grid lines which are defined by equally angled increments, the pseudo-polar grid lines are defined by an equally sloped increment of $\Delta s = 2/N$.

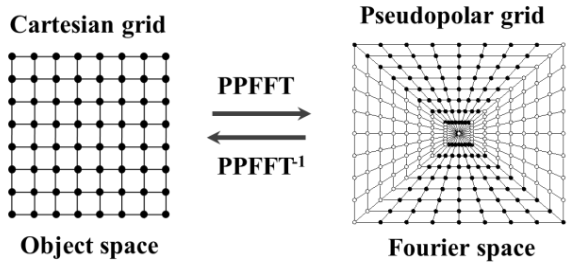

Fig. 2. Graphical construction of 2D PPFFT and its inversion. The object is an N×N pixel array in Cartesian grid, where N = 8. The Fourier space has 2N×2N points which are on a set of concentric squares (pseudo-polar grid). There are a total of 2N lines with each having 2N grid points and each line represents one piece of Fourier slice.

In order to match the angle of pseudo-polar grid, the projection angles are determined by $\theta = -\arctan((N+2-2n)/N)$ where $n = 1, 2, \ldots, N$ and $\theta = \pi/2 - \arctan((3N+2-2n)/N)$ where $n = N+1, N+2, \ldots, 2N$. As a result, the rotation angle varies from -45° to 135°. However, compared to the polar grid, the distance between sampling points along the lines of the pseudo-polar grid varies from line to line. To address this problem, the fractional Fourier transform (FrFT) can be utilized to vary the output sampling distance in Fourier space [16]. As a result, an equispaced data in a polar grid in object space can be mapped onto a specific line in the pseudo-polar grid in Fourier space. The 1D FrFT is defined as:

$$G_\theta(k) = \sum_{r=-N}^{N} g_\theta(r) e^{\left(-\frac{2\pi i \alpha k r}{2N}\right)}, -N \le k \le N, \quad (1)$$

where $G_\theta(k)$ is the Fourier transform of a given projection $g_\theta(r)$, θ is the projection angle, α is a parameter for the output sampling distance control. Note that Eq. (1) is equivalent to the forward Fourier transform when $\alpha = 1$ and the inverse Fourier transform when $\alpha = -1$. Choosing an appropriate α value, the object space projection data can be mapped to the grid points of any line in the pseudo-polar grid.

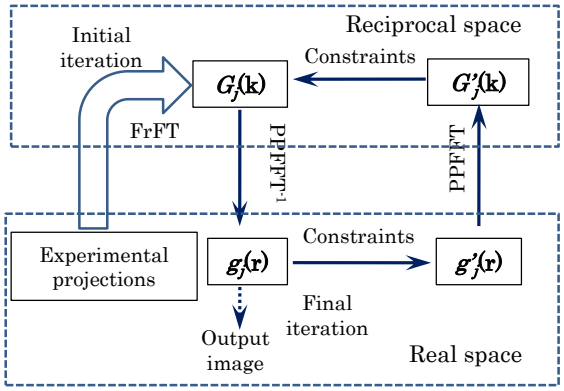

Fig. 3. Schematic layout of the iterative EST algorithm.

One solution for image reconstruction is to apply the inverse PPFFT directly. However, a strict requirement must be satisfied, that is, the number of projections needs to be 2N for an N×N object array. The EST algorithm overcomes this limitation by an iterative strategy which needs only about N/2 or even N/4 projections. First, the experimental projection data can be converted onto the pseudo-polar grid in Fourier space accurately by using FrFT, thereby all interpolations found in traditional reconstruction algorithms can be eliminated. Second, by using PPFFT and its inversion, the Fourier slice data are iterated back and forth between the Fourier and object domains, combining with some object and Fourier constraints. The Fourier constraints include replacing the calculated Fourier slices with the data from the corresponding experimental data. The object constraint is generally a boundary where the object is in. we set the values to zero outside this boundary. Fig. 3 shows the jth iteration of the algorithm. Once the final condition is satisfied (E.g. the maximum iteration time we set), the algorithm will produce the reconstructed image.

3. SIMULATION RESULTS

The EST method was firstly evaluated by simulation. As shown in Fig. 4, a digital head phantom was employed as the test sample and the projection sampling angle is equally sloped from -45° to 135°. Fig. 4 (b) shows the equally sloped sinograms. Notice that the sinograms for FBP reconstruction are equally angled, which is not shown here. Fig. 4 (c) demonstrates the reconstruction results of the FBP. In EST reconstruction, the object constraint was a rectangle with 380×460 pixels. After 20 iterations, the reconstruction was finally acquired, as shown in Fig. 4 (d).

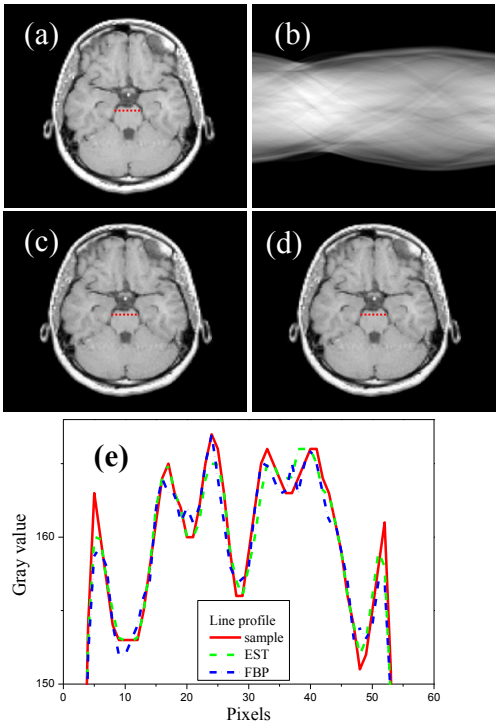

Fig. 4. Simulation results of a digital head phantom: (a) the original image, (b) the projection sequence from equally sloped angles (also called sinograms), (c) and (d) the tomographic reconstruction from the sinograms by FBP and EST, respectively, and (e) the line profiles of the 270th horizontal line in the phantom.

Benjamin compared EST and some other algorithms which indicated EST had great advantages in precision and the speed of convergence [17, 18]. In our simulation, we gave an example to verify the EST method. We used a digital head phantom as the original image. The image size is 512×512 pixels, and the number of projections for FBP was 512 while for EST it was 128. For a quantitative comparison, the reconstructed line profiles from FBP and EST are shown in Fig. 4 (e) at the 270th horizontal line in the phantom, which is marked as a red dashed line in Fig. 4(a), 4(c) and 4(d). The line profile of EST is more consistent with the sample compared to that of FBP, which indicates higher precision can be achieved. To verify this quantitatively, the root mean square error (RMSE) of the line profiles were calculated [19]. As shown in Fig. 4(e), the RMSE for EST was 1.1037 while that for FBP was 1.2461.

4. EXPERIMENTAL RESULTS

To test the feasibility on the *in-vivo* micro-CT, we took a live grasshopper as the sample. After anaesthetization, the sample was put into a tube. A millisecond shutter was used to control the exposure time and block the extra radiation. The X-ray was optimized at 11 keV according to the transmittance. Because the X-ray flux was too high, we put a 1 mm thick filter (Al filter) in X-ray beam upstream of the sample. The detector pixel size was 13 μm and the distance between the sample and detector (SDD) was 120 cm. 200 equally sloped projections were collected with each exposure time of 20 ms, so the total radiation time was about 4s. We calculated the radiation dose impacted on the sample, which was about 1.69Gy and the dose absorbed by the insect was about 0.67Gy [20]. The acquired images have 700×400 pixels, while the maximum width of the sample is about 460 pixels. So if we use equal angle tomographic method such as the FBP algorithm, about 720 projections were needed according to the sampling theorem, and the radiation dose would be 3.6 times higher.

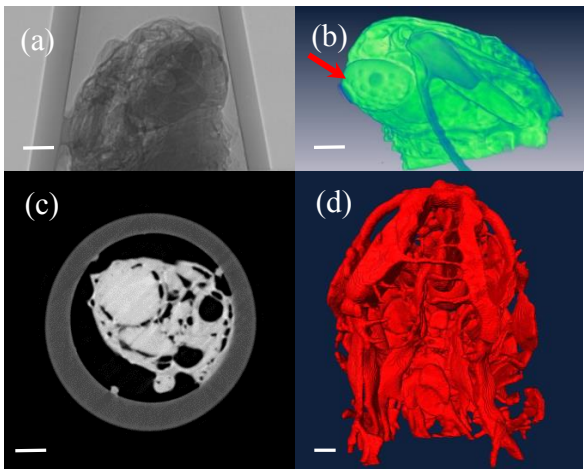

Fig. 5. In-vivo micro-CT for a grasshopper: a) one projection, b) 3D rendering, c) the 270th slice, and d) the structure of tubes inside of the grasshopper head. The scale bar is 1 mm.

The microstructure inside the sample was reconstructed using EST algorithm, as shown in Fig. 5. Before the EST reconstruction, the phase retrieval was performed (PITRE software, TIE-Hom phase retrieval algorithm with $\gamma = 500$) on each projection [21, 22], which was used to enhance the contrast of the tissue. Where $\gamma = \delta/\beta$, depending on the particular sample. This ratio is calculated according to the refractive index formula, $n = 1 - \delta + i\beta$, where δ is correlated with the phase, and β is correlated with the absorption [23]. They can be obtained from X-ray database [24]. Actually, the value of γ should be optimized during the phase retrieval and reconstruction processes. Fig. 5(a) is one projection of the grasshopper in which the structures at all

levels pack together. Fig. 5(b) is the 3D rendering of the grasshopper. The 270th slice is shown in Fig. 5(c), in which the networks of channels (the artery, tracheal tubes and some other tubes) are revealed clearly. As the arrow pointing to in Fig. 5 (b), the structure of the compound eye can be distinguished clearly. After image processing and segmentation, the 3D morphology of the networks of channels in the head of the grasshopper has been abstracted, as shown in Fig. 5(d). These channel networks are supposed to be the breathing channels of the grasshopper.

5. SUMMARY

In summary, the EST technique has been introduced into the *in-vivo* micro-CT. The simulation and experimental results demonstrate that the EST based low dose *in-vivo* micro-CT system with monochromatic synchrotron X-ray source, developed independently at BL13W1 of SSRF, is practicable. With the EST algorithm, the projection number and consequently the radiation dose can be greatly reduced. The results of this study illustrate that the micro-CT with synchrotron radiation X-rays is a potential tool for the investigation into the microstructure evolution inside a small animal such as an insect or a mouse for biomedical research. By upgrading the current sample stage and the detectors, it is possible to achieve dynamic micro-CT at 100~500 millisecond time scale. This means that the observation to the in situ or *in-vivo* dynamic evolution of microstructures will become practical for biomedical and material science.

6. ACKNOWLEDGMENT

This work was supported by the National Natural Science Foundation of China (Nos.31100680 and 81430087), the Joint Funds of the National Natural Science Foundation of China (No.U1232205), the CAS-CSIRO collaboration research project (No.GJHZ1303) and the Youth Innovation Promotion Association of CAS (No.2014235).

7. REFERENCES

[1] R.C. Chen, L. Ping, T.Q. Xiao, and L.X. Xu, "The X-ray imaging for nondestructive microstructure analysis at SSRF", *Advanced Materials* **26**, 7688(2014).

[2] Y.J. Guan, Y.T. Wang, F.L. Yuan, H.Y. Lu, Y.Q. Ren, T.Q. Xiao, K.M. Chen, D.A. Greenberg, K.L. Jin, and G.Y. Yang, "Effect of Suture Properties on Stability of Middle Cerebral Artery Occlusion Evaluated by Synchrotron Radiation Angiography", *Stroke* **43,** 888(2012).

[3] X.S. Zhang, G.Y. Peng, G.H. Du, X.C. Sun, G.H. Jiang, X.M. Zeng, P.F. Sun, B. Deng, H.L. Xie, Z.J. Wu, and T.Q. Xiao , "Investigating the microstructures of piston carbon deposits in a large-scale marine diesel engine using synchrotron X-ray microtomography", *Fuel*. **142,** 173(2015).

[4] R.C. Chen, L. Kigon, and R. Longo, "Comparison of single distance phase retrieval algorithms by considering different object composition and the effect of statistical and structural noise", *Opt. Express* **21,** 7384 (2013).

[5] H.Q. Liu, Y.Q. Ren, H. Guo, Y.L Xue, H.L Xie, T.Q Xiao, and X.Z Wu, "Phase retrieval for hard X-ray computed tomography of samples with hybrid compositions", *Chin. Opt. Lett*. **10,** 121101 (2012).

[6] R.C. Chen, H.L. Xie, L. Rigon, R. Longo, E. Castelli, and T.Q. Xiao, "Phase retrieval in quantitative x-ray microtomography with a single sample-to-detector distance", *Opt. Lett*. **36,** 1719 (2011).

[7] D. Cavanagh, E. Johnson, R. Price, J. Kurie, E. Travis and D. Cody, "In vivo respiratory gated micro-CT imaging in small-animal oncology models", *Mol. Imag*. **3**, 55 (2004).

[8] T. Rolo, A. Ershov, T. kamp, and T. Baumbach, "In vivo X-ray cine-tomography for tracking morphological dynamics", *PNAS*. **111,** 3921 (2014).

[9] S. Dubsky, S. Hooper, K. Siu and A. Fouras, "Synchrotron-based dynamic computed tomography of tissue motion for regional lung function measurement", *J. R. Soc, Interface*, **9**, 2213 (2012).

[10] T. Sera, H. Yokota, K. Uesugi and N. Yagi, "Airway distension during lung inflation in healthy and allergic-sensitised mice in vivo", *Resp. Physiol. Neurobi*. **185,** 639 (2013).

[11] J.W. Miao, F. Förster, and O. Levi, "Equally sloped tomography with oversampling reconstruction", *Phys. Rev.* B **72,** 052103 (2005).

[12] Y.Z. Zhao, E. Brun, P. Coan, Z.F. Huang, A. Sztrókay, P.C. Diemoz, S. Liebhardt, A. Mittone, S. Gasilov, J.W. Miao, and A. Bravin, "High-resolution, low-dose phase contrast X-ray tomography for 3D diagnosis of human breast cancers", *PNAS* **109,** 18290 (2012).

[13] S.K. Yao, J.D. Fan, Y.B. Zong, Y. He, G.Z. Zhou, Z.B. Sun, J. H. Zhang, Q.J. Huang, T.Q. Xiao and H.D. Jiang, "Equally sloped X-ray microtomography of living insects with low radiation dose and improved resolution capability", *Appl. Phys. Lett*. **108** 123702 (2016).

[14] H.L. Xie, B. Beng, G.H. Du, Y.N. Fu, Y. He, H. Guo, G.Y. Peng, Y.L. Xue, G.Z. Zhou, Y.Q. Ren, Y.D. Wang, R.C. Chen, Y.J. Tong, and T.Q. Xiao, "X-ray biomedical imaging beamline at SSRF", *J. Instrum*. **8,** C08003 (2013).

[15] A. Averbuch, R.R. Coifman, D.L. Donoho, M. Elad, and M. Israeli, "Fast and accurate Polar Fourier transform", *Appl. Comput. Harmon. Anal*. **21,** 145(2006).

[16] D.H. Bailey, P.N. Swarztrauber, "Fractional Fourier transform and applications", *SIAM Rev.* **33,** 389 (1991).

[17] F. Benjamin, Y. Mao, P. Cloetens and J.W. Miao, "Low-dose x-ray phase-contrast and absorption CT using equally sloped tomography", *Phys. Med. Biol.* **55**, 5383 (2010).

[18] F. Benjamin, Y.Z Zhao, Z.F. Huang, R. Fung, Y. Mao, C. Zhu, K. Maryam, J. DeMarco, J. Stanley, F. Michael and J.W Miao, "Radiation dose reduction in medical x-ray CT via Fourier-based iterative reconstruction", *Med. Phys.* **40**,031914 (2013).

[19] M. Anderson and W. Woessner, Applied Groundwater Modeling: Simulation of Flow and Advective Transport (Academic Press, 1992).

[20] M. Torikoshi, Y. Ohno, N. Yagi, K. Umetani, and Y. Furusawa, "Dosimetry for a microbeam array generated by synchrotron radiation at SPring-8", *EJR* **68,** S114 (2008).

[21] D. Paganin and K. Nugent, "Phase measurement of waves that obey nonlinear equations", *Opt. Lett*. **27,** 622 (2002).

[22] R.C. Chen, D. Dreossi, L. Mancini, R. Menk, L. Rigon, T.Q. Xiao, and R. Longo, "PITRE: software for phase-sensitive X-ray image processing and tomography reconstruction", *J. Synchrotron Radiat.* **19**, 836 (2012).

[23] X.Z. Wu, H. Liu, and A.M. Yan, "X-ray phase-attenuation duality and phase retrieval", *Opt. Lett.* **30**, 379 (2005).

[24] CXRO, Web Site: http://henke.lbl.gov/optical_constants/getdb2.html (2012).